ADVANCED FUNCTIONAL MATERIALS
www.afm-journal.de

Materials Views
www.MaterialsViews.com

Carbon Nanotube-Encapsulated Noble Metal Nanoparticle Hybrid as a Cathode Material for Li-Oxygen Batteries

Xin Huang, Hong Yu, Huiteng Tan, Jixin Zhu, Wenyu Zhang, Chengyuan Wang, Jun Zhang, Yuxi Wang, Yunbo Lv, Zhi Zeng, Dayong Liu, Jun Ding, Qichun Zhang, Madhavi Srinivasan, Pulickel M. Ajayan, Huey Hoon Hng,* and Qingyu Yan**

Although Li-oxygen batteries offer extremely high theoretical specific energy, their practical application still faces critical challenges. One of the main obstacles is the high charge overpotential caused by sluggish kinetics of charge transfer that is closely related to the morphology of discharge products and their distribution on the cathode. Here, a series of noble metal nanoparticles (Pd, Pt, Ru and Au) are encapsulated inside end-opened carbon nanotubes (CNTs) by wet impregnation followed by thermal annealing. The resultant cathode materials exhibit a dramatic reduction of charge overpotentials compared to their counterparts with nanoparticles supported on CNT surface. Notably, the charge overpotential can be as low as 0.3 V when CNT-encapsulated Pd nanoparticles are used on the cathode. The cathode also shows good stability during discharge–charge cycling. Density functional theory (DFT) calculations reveal that encapsulation of "guest" noble metal nanoparticles in "host" CNTs is able to strengthen the electron density on CNT surfaces, and to avoid the regional enrichment of electron density caused by the direct exposure of nanoparticles on CNT surface. These unique properties ensure the uniform coverage of Li_2O_2 nanocrystals on CNT surfaces instead of localized distribution of Li_2O_2 aggregation, thus providing efficient charge transfer for the decomposition of Li_2O_2.

1. Introduction

The exceptionally high theoretical specific energy density of rechargeable Li-O_2 batteries (up to 2–3 kW h kg^{-1}) rivaling that of any other existing rechargeable batteries has triggered tremendous research interest in pursuit of technological breakthrough to commercialize this energy storage system.[1–13] In the non-aqueous Li-O_2 batteries, the energy storage mechanism is based on the oxygen reduction reaction (ORR) and oxygen evolution reaction (OER) according to this equation: $2(Li^+ + e) + O_2 \leftrightarrow Li_2O_2$ (E_0 = 2.96 V vs Li/Li$^+$).[7–9] During the discharging process, ORR takes place to form the poor electrical conductive Li_2O_2 solids as the discharge products. Although the inverse OER decomposes the Li_2O_2 solids during the charging process, the slow charge transfer of Li_2O_2 solids results in electrode polarization, making the high charge

---

Dr. X. Huang
Department of Biomass and Chemical Engineering
Sichuan University
Chengdu 610065, PR China
E-mail: xhuangscu@163.com

Dr. X. Huang
National Engineering Laboratory for Clean
Technology of Leather Manufacture
Sichuan University
Chengdu 610065, PR China

Dr. H. Yu, Dr. H. Tan, Dr. J. Zhu, Dr. W. Zhang,
Dr. C. Wang, Prof. Q. Zhang, Prof. M. Srinivasan,
Prof. H. H. Hng, Prof. Q. Yan
School of Materials Science and Engineering
Nanyang Technological University
50 Nanyang Avenue 639798, Singapore
E-mail: alexyan@ntu.edu.sg; ashhhng@ntu.edu.sg

Prof. P. M. Ajayan
Department of Mechanical Engineering
& Materials Science
Rice University
Houston, Texas 77005, USA

Dr. Y. Wang
CREATE, #10–02 1 CREATE Tower
138602, Singapore

Dr. J. Zhang, Prof. Z. Zeng, Prof. D. Liu
Institute of Solid State Physics
Chinese Academy of Sciences
350 Shushanghu Road, Hefei 230031, Anhui, PR China

Prof. Q. Yan
Energy Research Institute @ Nanyang
Technological University
Nanyang Technological University
50 Nanyang Avenue 639798, Singapore

Dr. Y. Lv, Prof. J. Ding
Department of Materials Science & Engineering
National University of Singapore
7 Engineering Drive 1 117574, Singapore

DOI: 10.1002/adfm.201400921

overpotential that associated with sluggish charge transfer kinetics one of the critical issues for its realization.[10–12]

A variety of materials has been investigated as catalysts to enhance the OER activity. Early studies primarily focused on carbonaceous materials and transition-metal oxides (α-MnO_2 and Co_3O_4 etc.) using carbonate-based electrolytes, but poor OER activity with charge potential high up to 4.5 V was shown.[13–16] Although successful attempts were subsequently made on reducing the charge overpotential employing noble metals (Au, Pt and Ru etc.) as the catalysts in carbonate-based or mixture of carbonate/ether electrolytes,[1,9,17–20] problems remain. For instances, Harding et al.[19] found that Au/C catalyst could only be OER active at voltage higher than 4.0 V, while Pt/C might catalyze the electrolyte decomposition. Additionally, McCloskey et al.[20] reported that the OER performance of Au nanoparticles was similar to carbon in dimethoxyethane (DME)-based electrolyte.

Although much effort has been devoted to exploring efficient OER catalyst for non-aqueous Li-O_2 battery, fundamentals on rational catalyst design are still lack of in-depth understandings. In this regard, we were particularly intrigued by the theoretical studies conducted by Norskov et al.,[21] revealing that the charge overpotentials for Li_2O_2 can be as low as 0.2 V if the charge transfer involved is not impeded during charging. Some reports also showed that limitations in charge transport of OER are close related to the morphology of Li_2O_2 and their distribution on the cathode.[6,22,23] Considering that ORR is an electron-induced process,[24] the surface electron state of cathode materials has pronounced influence on the formation of Li_2O_2. From this point of view, the kinetics of charge transfer during charging could be improved accordingly by tuning the surface electronic state of cathode materials, providing a solution to reduce the charge overpotential by optimizing the morphology and distribution of Li_2O_2 on the cathode. Unfortunately, conventional cathodes are typically made from directly mixing of carbon materials with catalyst nanoparticles.[2,10,25–27] On discharge, the catalyst nanoparticles serve as "active seeds" for the initial nucleation of Li_2O_2. Continuous growth of Li_2O_2 on these seeds eventually leads to the formation of Li_2O_2 particles covering the active nanoparticles. The low Li_2O_2 coverage region might induce localized distribution of Li_2O_2 on the cathode, and eventually leading to electrode polarization. Due to the poor conductive nature of Li_2O_2, it is much difficult to decompose the Li_2O_2 that are remote from the cathode surface as compared to those have intimate contact with the cathode surface.[28] Therefore, although Li_2O_2 can themselves be oxidized as shown by modeling calculations, high charge overpotentials are usually evidenced on various cathodes even at low discharge depth. Obviously, the regional enrichment of electron density caused by the direct exposure of catalyst nanoparticles is one of the major reasons that are responsible for the localized distribution of discharge products. To tackle this problem, one possible solution is to suppress the regional enrichment of electron density on the cathode surface. However, rational design of such "ideal" cathode remains a great challenge.

Carbon nanotubes (CNTs) are known as efficient ORR catalysts, but they have little OER activity.[29–31] However, as noted above, it is possible to enable the decomposition of Li_2O_2 on CNTs with low charge overpotential by tuning the surface electronic state of CNTs. Confinement of nanoparticles (NPs) inside the channels of CNTs has been shown to significantly change the electrochemical properties of both CNTs and encapsulated NPs.[32,33] However, less attention has been paid to the modulated π electrons on CNTs surface, especially for applying to the electrochemistry of Li-O_2 battery. In fact, it is feasible to strengthen the electron density of CNTs by encapsulating "guest" NPs inside, making the electron-induced ORR more favorable on the surfaces of the "host" CNTs via the electronic interactions between the encapsulated NPs and the curved graphene walls. Most importantly, the encapsulation of NPs eliminates localized electron density enrichment derived from the direct exposure of catalyst nanoparticles, and hence, the nucleation of Li_2O_2 could be promoted on the entire CNTs surfaces rather than on specific catalytic regions. As a result, the sluggish kinetics of charge transfer in OER could be greatly improved in the absence of localized distribution of Li_2O_2, endowing the OER with lower charge overpotential. In the present study, we prepared a series of carbon nanotubes-encapsulated noble metal nanoparticles, and systematically investigated their performances in Li-oxygen batteries. As expected, the as-prepared hybrid materials exhibited superior OER activity than the conventional cathodes materials with noble metal nanoparticles direct supported on CNTs, thus demonstrating the feasibility of our strategy.

2. Results and Discussion

We encapsulated a series of noble metal NPs within CNTs, including Pd, Ru, Pt and Au. The CNTs-encapsulated noble metal nanoparticles are denoted as MNPs@CNTs. These hybrid materials were prepared by a two-step synthetic approach, which included wet impregnation and thermal annealing (details shown in the experimental section). The pristine CNTs were firstly ball milled into end-opened nanotubes (Figure S1) and then soaked in the precursor solutions. During the impregnation, the precursor solutions fill the end-opened CNTs by capillary forces. Subsequently, they were converted into the corresponding metallic NPs by thermal treatment in Ar/H_2. The high resolution transmission electron microscopy (HRTEM) images of PdNPs@CNTs shown in **Figure 1**a clearly illustrate the open-ended feature of CNTs and small PdNPs encapsulated within these nanochannels. Here, the growth of PdNPs is restricted by the dimension of the CNTs nanochannel, giving rise to particle size of 2.5 ± 0.5 nm. Additionally, the encapsulated PdNPs are uniformly distributed in CNTs without severe aggregation. The highly crystalline nature of the PdNPs is manifested by having distinct lattice spacing of 2.24 Å that corresponds to {111} plane (the inset in Figure 1a). Other noble metal NPs (Figure 1b-d), including RuNPs, PtNPs and AuNPs are also successfully encapsulated in CNTs, and the corresponding particle diameters are 2.7 ± 0.5 nm, 1.8 ± 0.5 nm and 3.0 ± 0.5 nm, respectively. Detailed TEM observations by rotating the specimen in the electron microscope were also carried out to confirm the encapsulation of NPs inside CNTs (Figure S2). The crystal structures of MNPs@CNTs are further confirmed by wide-angle XRD (Figure S3). For comparison, CNTs-supported noble metal nanoparticles (MNPs-CNTs) were

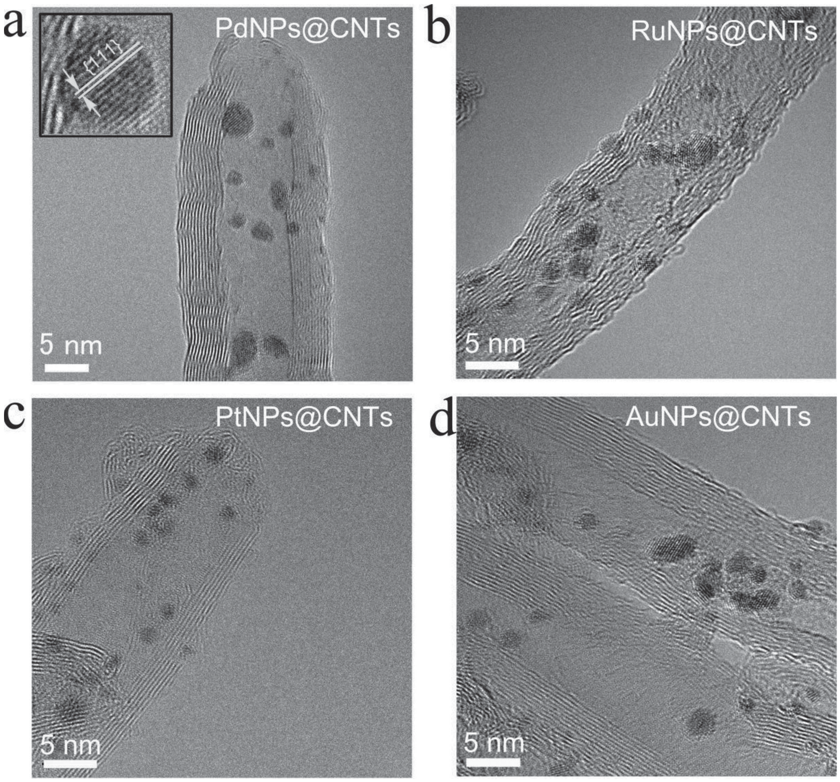

Figure 1. Microstructure of MNPs@CNTs. (a) HRTEM image of PdNPs@CNTs with PdNPs (2.5 ± 0.5 nm) located on the interior multiple carbon wall. The inset shows clear lattices of PdNPs, corresponding to the {111} plane of Pd. HRTEM images of (b) RuNPs@CNTs, (c) PtNPs@CNTs and (d) AuNPs@CNTs, and the corresponding diameters of the encapsulated NPs are 2.7 ± 0.5 nm, 1.8 ± 0.5 nm and 3.0 ± 0.5 nm respectively.

also prepared, where the noble metal NPs were directly supported on the pristine CNTs (Figure S4).

In the Raman spectrum, G band of CNTs that associated with the sp^2 hybridization of carbon is sensitive to charge transfer. The occurrence of charge transfer usually leads to resonance frequency shift in G band,[34,35] making it a powerful tool to determine the charge donating or accepting behaviors of CNTs in response to different environments. **Figure 2**a shows the Raman spectra of the end-opened CNTs and MNPs@CNTs. The G band of CNTs is located at 1589 cm^{-1} while the G band of CNTs with the encapsulation of noble metal NPs shows a red shift. Additionally, no shift is observed for end-opened CNTs after thermally treated in Ar/H$_2$ (Figure S5). These results suggest that the electrons are being transferred from the noble metal NPs to CNTs. Taking PdNPs@CNTs as an example, the G band shifts from 1589 to 1575 cm^{-1}. These results are also consistent with the XPS analyses (Figure 2c). The C–C peak of CNTs that located at 285.1 eV shifts to lower binding energy of 284.8 eV after the encapsulation with PdNPs, while the Pd *3d* spin splitting peaks also appear at higher binding energy (336.1 and 341.3 eV) compared to that of usually reported metallic Pd (Figure S6).[36,37] Similarly, C *1s* peaks for all other MNPs@CNTs samples also shift to lower binding energy due to the electron-donating effect (Figure 2c). For the MNPs-CNTs (Figure 2b), the electron donation from the supported noble metal NPs can still be perceived by having a red shift in G band of Raman spectra as compared to pristine CNTs, suggesting the electron still donated from noble metal NPs to CNT in MNPs-CNTs.

Li-O$_2$ battery performances were carried out (Figure S7), and the discharge capacity was first fixed to 250 mAh g^{-1} to investigate the OER activity. In Figure S8, the pristine CNTs exhibit a high charge potential of ~4.5 V with a charge overpotential of ~1.5 V (compared to the theoretical charge potential

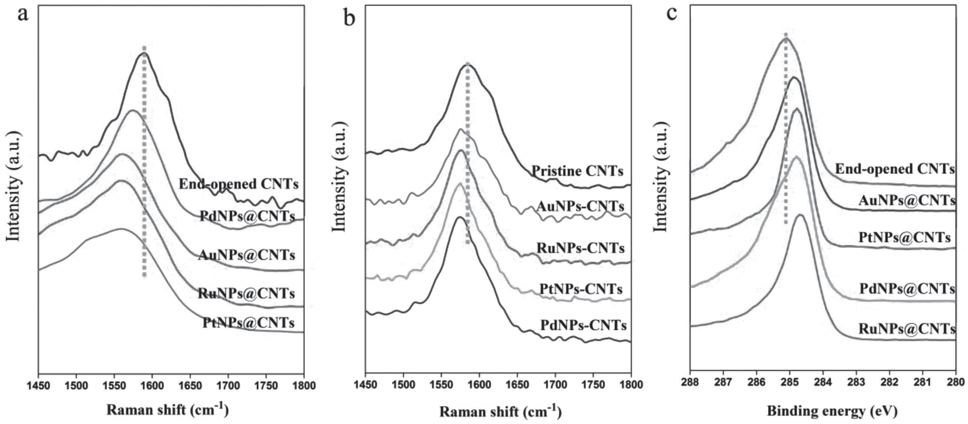

Figure 2. Electronic interactions between encapsulated/supported NPs with CNTs. (a) Raman spectra of end-opened CNTs and MNPs@CNTs. The G band of CNTs (1589 cm^{-1}) associated to SP^2 hybridization of carbon shows red shift after the encapsulation of noble metal NPs. (b) Raman spectra of pristine CNTs and MNPs-CNTs. The G band of CNTs also exhibits red shift as compared to the pristine CNTs. (c) C *1s* XPS spectra of end-opened CNTs and MNPs@CNTs. After the encapsulation of noble metal NPs, all the C *1s* peak of MNPs@CNTs move to lower binding energy, suggesting the electron transfer to C atom of CNTs.

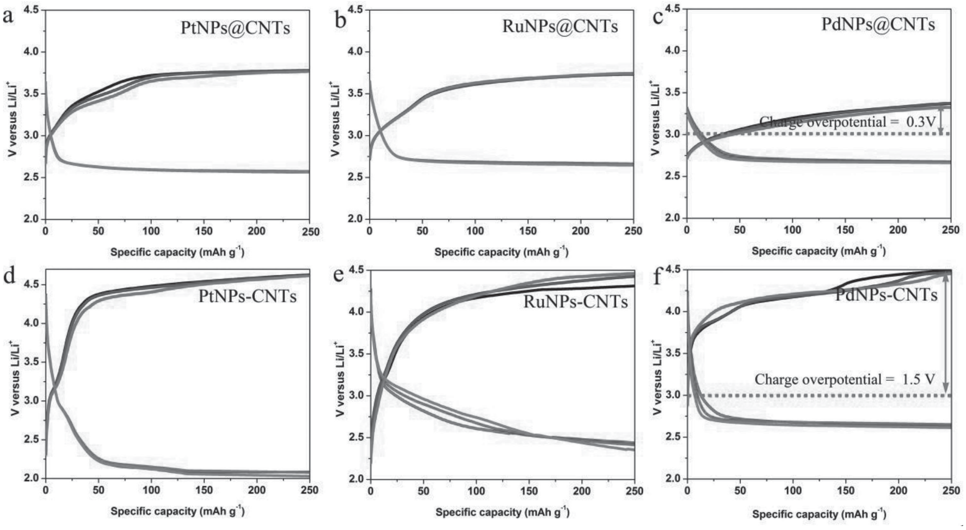

Figure 3. Voltage profiles of cathode materials with discharge capacity of 250 mAh g^{-1}. Voltage profiles during initial 3 discharge-charge cycles of cells (to 250 mAh g^{-1}) based on (a) PtNPs@CNTs, (b) RuNPs@CNTs, (c) PdNPs@CNTs, (d) PtNPs-CNTs, (e) RuNPs-CNTs and (f) PdNPs-CNTs.

of 3.0 V). For the end-opened CNTs, the high charge overpotential is still observed (Figure S8), which eliminates the influence of ball milling on the battery performances of MNPs@CNTs. Compare to CNT and end-opened CNTs, the MNPs@CNTs exhibit a considerable decrease in charge potentials (**Figure 3**a-c and Figure S9). With the encapsulation of PdNPs, RuNPs, PtNPs and AuNPs, the charge potentials are dramatically decreased to 3.3 V, 3.6 V, 3.8 V and 4.2 V, respectively. Notably, the charge overpotential of PdNPs@CNTs is as low as 0.3 V, which is close to the theoretical value (~0.2 V),[21] and it remains almost constant after 20 cycles (Figure S10). However, MNPs-CNTs exhibit much poor OER activity compared to MNPs@CNTs. Although the electron density of CNTs is also substantially strengthened in MNPs-CNTs, high charge potentials are still pertained (Figure 3d-f and Figure S9), which are 4.6, 4.4, 4.5 and 4.4 V for PtNPs-CNTs, RuNPs-CNTs, PdNPs-CNTs and AuNPs-CNTs, respectively. In this regard, the charge potentials of MNPs-CNTs are almost equal to that of pristine CNTs (4.5 V).

To confirm the discharge products on the cathode materials, ^{1}H NMR, XRD and Raman analyses were carried out. As shown in Figure S11a-d, the peak of CH_3CO_2Li is quite small in the NMR spectra of MNPs@CNTs after discharge.[38,39] In Figure S11i-l, the peak intensity of CH_3CO_2Li shows no significant change after charge. As we know, carbon oxidizes above 4 V versus Li/Li$^+$.[38] For the MNPs@CNTs (Pd, Pt and Ru), their charge potentials do not exceed 4 V. Hence, the discharge capacity of MNPs@CNTs should not be mainly based on the electrolyte decomposition although the electrolyte decomposition is indeed involved (the small peak of CH_3CO_2Li). XRD (Figure S12) and Raman analyses (Figure S13) further confirm that Li_2O_2 are the dominant discharge products on MNPs@CNTs.[2] Hence, the performance of MNPs@CNTs-based Li oxygen batteries should be mainly based on the reversible formation/decomposition of Li_2O_2. For the MNPs-CNTs, the peak of CH_3CO_2Li is observed in the NMR spectra after discharge. After charge, the peak intensity of CH_3CO_2Li is decreased. These changes suggest that compared with MNPs@CNTs, the higher charge overpotential of MNPs-CNTs can be partially attributed to the decomposition of CH_3CO_2Li.

Subsequently, we further focused on the nucleation and morphological evolution effect of Li_2O_2 on the charge overpotential. The investigations to the morphology of Li_2O_2 at low discharge capacity (250 mAh g^{-1}) are essential to reveal the growth mechanism of Li_2O_2 on the electrodes. These can tell us the discharge behaviors are how different between MNPs-CNTs and MNP@CNTs at the initial stage. For pristine CNTs (in **Figure 4**a,b) after discharge, non-homogeneous distribution of Li_2O_2 are observed as compared with the fresh CNTs (Figure S14), where Li_2O_2 particles (300~500 nm) tend to undergo self-aggregation rather than evenly distribute on the surface of CNTs. The Li_2O_2 particles have limited contact with CNTs, and majority of the CNTs have smooth surfaces without coverage of Li_2O_2. The observed morphologies are consistent with other reported CNTs-based cathodes.[23] The nucleation of Li_2O_2 on pristine CNTs is likely to be initiated at specific regions (electron-enriched areas) rather than on whole CNTs surfaces. Charging these aggregated particles of Li_2O_2 that are remote from the CNTs should be very difficult and require high charge potential. For the MNPs@CNTs, they show differences in morphology after discharge. Figure 4c, d show rough surfaces of worm-like morphology without observing any large isolated Li_2O_2 particles for RuNPs@CNTs after discharge. It is plausible to assume that the nucleation and simultaneous growth of Li_2O_2 occur homogeneously on the whole CNTs surface rather than solely occur on specific catalyst regions. This hypothesis is further supported by TEM observation of RuNPs@CNTs at the end of discharge (Figure S15), where the surface of CNTs is covered by Li_2O_2. For PtNPs@CNTs after discharge (Figure S16), their morphologies are similar to those of RuNPs@CNTs after discharge, showing no localized distribution of Li_2O_2 particles or "inert" CNTs (without the coverage of Li_2O_2). On PdNPs@CNTs (Figure S17) after discharge, intensive growth of Li_2O_2 nuclei on CNTs results in packed Li_2O_2 nanocrystals (~10 nm)

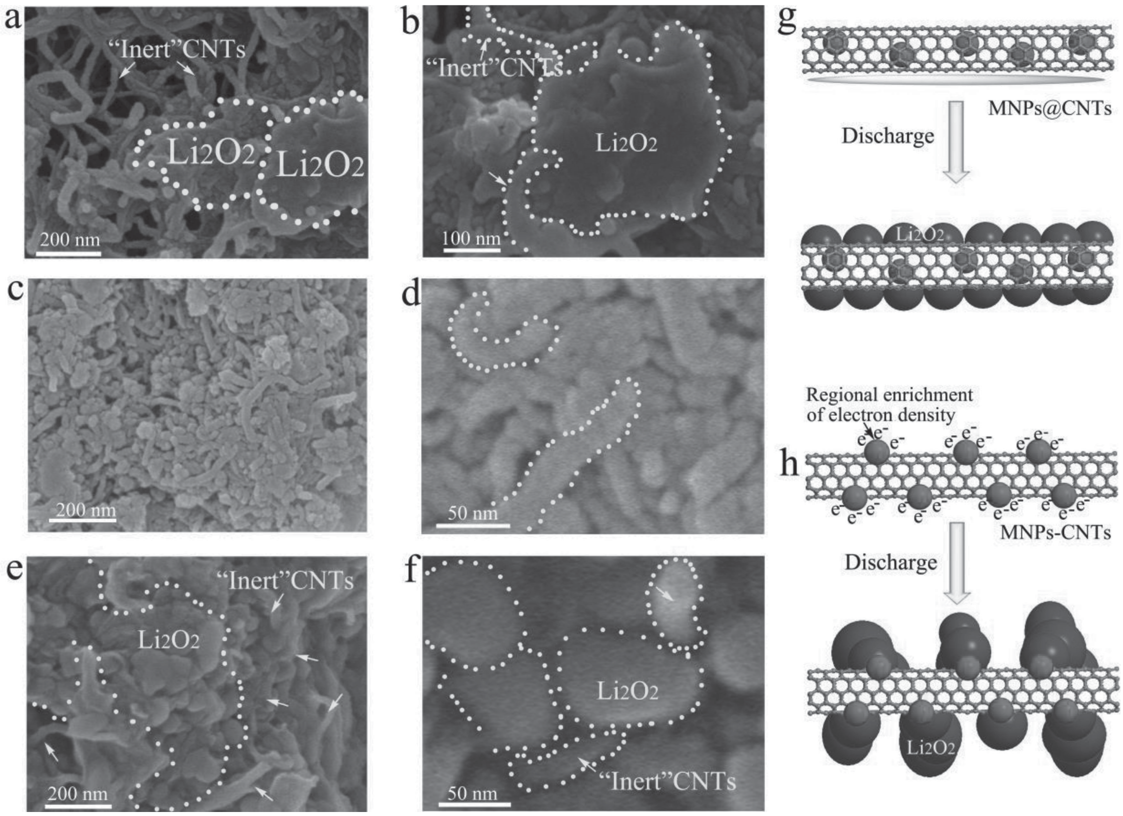

Figure 4. Morphology of the cathode materials after discharge, and the proposed mechanism for Li_2O_2 nucleation on MNPs@CNTs and MNPs-CNTs. SEM images of (a, b) pristine CNTs, (c, d) RuNPs@CNTs and (e, f) RuNPs-CNTs after 10th cycle discharged to 250 mAh g^{-1}. (g, h) Proposed mechanism for Li_2O_2 nucleation on MNP@CNTs and MNP-CNTs. For MNP@CNTs, the surface electron density is strengthened, where the nucleation and growth of Li_2O_2 is promoted on the entire CNTs surface. For MNP-CNTs, the regional enrichment of electron density around noble metal NPs leads to localized distribution of Li_2O_2 aggregation on the exposed noble metal NPs.

covering the initial growth layer of worm-like Li_2O_2. These observations suggest that the problem of localized Li_2O_2 distribution on CNTs is alleviated, and the contact at Li_2O_2/CNTs interfaces is improved. In the SEM images of MNPs-CNTs after discharge (Figure 4e, f and Figure S18 and S19), the localized aggregation of Li_2O_2 particles still have limited contact with CNTs, although the particle size of Li_2O_2 (100~200 nm) is reduced compared with pristine CNTs after discharge. It should be noted that the morphology of Li_2O_2 may be influenced by the discharge rate and the formation of by-product, such as CH_3COOLi. However, in the present investigation, However, in the present investigation, the discharge rates are kept the same for both MNPs-CNTs and MNPs@CNTs (50 mA g^{-1}), and Li_2O_2 are the main discharge products (as shown by XRD and Raman analyses). Thus, the morphology differences among these two types of electrodes should not be caused by the influence of discharge rate or the formation of other by-products.

The mechanism for Li_2O_2 nucleation on MNPs@CNTs is proposed and illustrated in Figure 4g, where the encapsulation of noble metal NPs in CNTs strengthens the density of π electron on entire CNTs surface. Without exposure of noble metal NPs as "active seeds" for localized nucleation of Li_2O_2, the nucleation and growth of Li_2O_2 would occur homogeneously on the whole CNTs. Hence, the worm-like morphology with rough surface can be observed on at the discharge depth of 250 mAh g^{-1}. Although stoichiometric Li_2O_2 is a bulk insulator with a bandgap ≥1.88 eV,[40] O-rich facets of Li_2O_2 may provide surface pathways for electron transport.[40,41] On MNPs-CNTs, the Li_2O_2 nanocrystals formed have large surface area, so the surface electronic conductivity is highly beneficial for the electrochemical reduction of small Li_2O_2 particles. Additionally, the intimate contact of Li_2O_2 nanocrystals with CNTs also facilitates charge transfer at Li_2O_2/CNTs interfaces, thus substantially reducing the charge overpotential caused by the sluggish charge transfer.

After discharge, a considerable amount of "inert" CNTs appears on MNPs-CNTs but rarely observed on MNPs@CNTs. These results strongly indicate that although electron transfer is essential for CNTs to improve the activity of electron-induced ORR, supporting electron-rich species (especially for noble metals NPs) on CNTs induce regional enrichment of electron density. When oxygen is adsorbed on these regions,[6,42] the enriched electrons induce preferential growth of Li_2O_2 (in Figure 4h), resulting in severe electrode polarization. In addition to the decomposition of Li_2CO_3 on charge, the localized distribution of Li_2O_2 could be another underlying reason for having high charge potential on MNPs-CNTs. To get a better insight into this issue, DFT calculations were carried out. We simplified the system by encapsulating a single Pd (Pt) atom (Pd_1/Pt_1) within end-opened single wall CNT (5, 5) (inset I-III

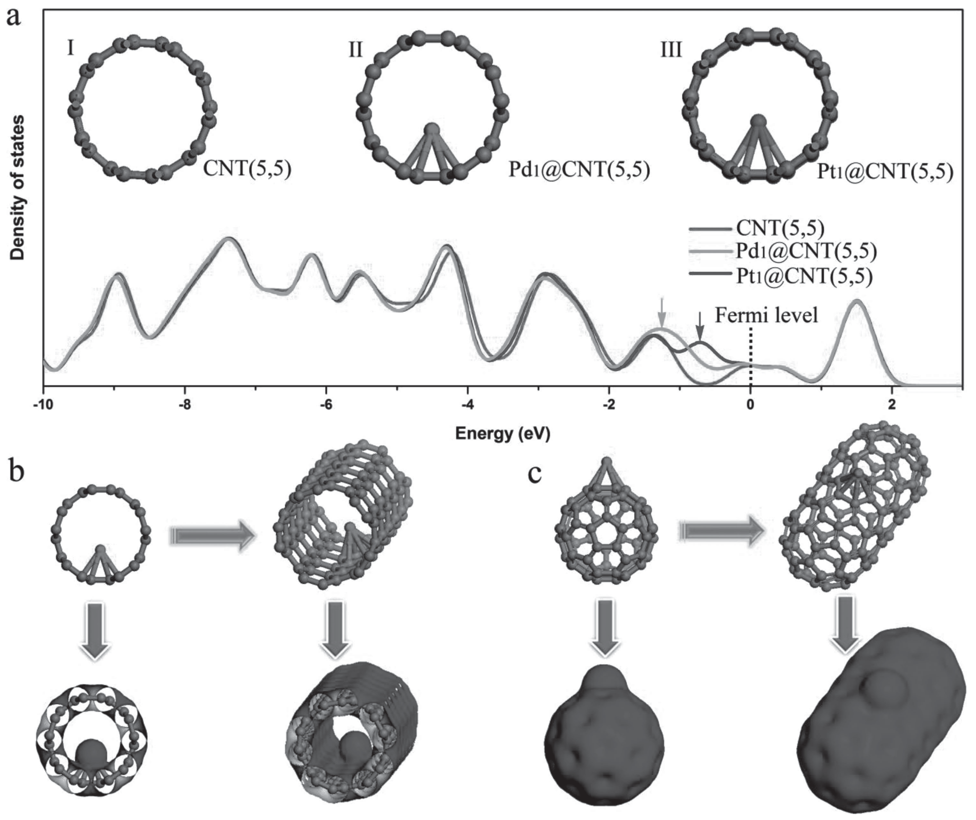

Figure 5. Results of DFT calculations. (a) DOS of end-opened CNT (5, 5), Pd_1@CNT(5, 5) and Pt_1@CNT (5, 5). The Fermi level is aligned at 0 eV. Inserted plot I, II and III illustrate the structure of CNT (5, 5), Pd_1@CNT (5, 5) and Pt_1@CNT (5, 5), respectively. (b) Pd_1@CNT (5, 5) and its electron density distribution. The electron density on the surface of CNT (5, 5) is isotropically distributed along the longitude axis of CNT (5, 5). (c) Pd_1-CNT (5, 5) and its electron density distribution. The spherical electron cloud of Pd_1 is raised above the tubular electron cloud surrounding the CNT (5, 5) surface.

in **Figure 5**a) or bonding them to the surface of end-sealed CNT (5, 5) (Figure S20).

Figure 5a shows the projected density of states (DOS) of CNT (5, 5), Pd_1@CNT (5, 5) and Pt_1@CNT (5, 5). DOS of CNT (5, 5) is modified by the encapsulation of Pd_1 and Pt_1 in the low-DOS region near the Fermi level from 0 to –1.3 eV. The DOS of Pt_1@CNT (5, 5) shows a new peak at –0.68 eV compared to CNT (5, 5). For Pd_1@CNT (5, 5), the intensity of DOS at –1.28 eV is higher than that of CNT (5, 5). These changes suggest the occurrence of electron transfer to CNT. Based on Mulliken population analyses (Table S21), encapsulated Pd_1 donates more electrons (0.204 electrons) to CNT than the encapsulated Pt_1 (0.122 electrons). The surface bound Pd_1 donates even more electrons (0.228 electrons) than the capsulated Pd_1. Based on density functional theory (DFT) calculations conducted by Xu et al.,[43] the ORR activity is closely related to the carbon type and its electronic structure. Hence, the encapsulation of metal nanoparticles in CNTs can influence their ORR activity. Deng and coworkers have compared the ORR activity of CNTs and CNTs-encapsulated Fe according to the theoretical calculations.[44] In their work, the encapsulation of Fe indeed promotes the ORR activity of CNTs by decreasing the work function of O_2 absorbed on the CNTs surface. In the present investigation, our DFT calculations have confirmed the electron donation from noble metal to CNTs. Considering that the discharge process of Li-oxygen batteries also belongs to ORR, it is thus reasonable that the nucleation in ORR should be promoted on MNPs@CNTs (M = Pd and Pt) as compared with CNTs. It should also be noted that the localized enrichment of surface electron density is involved in Pd_1-CNT (5, 5) (Figure 5c), where spherical electron cloud of surface bound atom is raised above the tubular electron cloud surrounding the CNT (5, 5) surface. In contrast, encapsulation strategy completely eliminates the anisotropic distribution of surface electrons. The electron clouds on the surface of Pd_1@CNT (Figure 5b) are still uniformly distributed along the longitude axis of CNT (5, 5). Similar phenomena are also observed in Pt_1-CNT (5, 5) and Pt_1@CNT (5, 5) (Figure S22). Hence, the most distinct advantage of the encapsulation strategy is the strengthening of surface electron density of CNTs without suffering localized enrichment of surface electron density, which is a major reason responsible for the uniform coverage of Li_2O_2 observed in above SEM images.

We also found that the electronegativity of encapsulated noble metal NPs has close correlation to the OER activity of MNPs@CNTs. The sequence of electronegativity for the investigated noble metals are as follows: Au (2.54) > Pt (2.28) > Ru (2.2) = Pd (2.2) and their OER activities obey this order: PdNPs@CNTs > RuNPs@CNTs > PtNPs@CNTs > AuNPs@CNTs. Normally, metal will readily to give more electrons with decrease in electronegativity. Thus, Pd/Ru with the lowest electronegativity should donate the most electrons, followed by Pt, and Au with the highest electronegativity donates the least electrons. The above Mulliken population analyses show that encapsulated Pd_1 (0.204 electrons) donates more electrons than the encapsulated Pt_1 (0.122 electrons). Thus, the order of strengthened surface electron density on MNPs@CNTs is highly consistent with their OER activity. These results effectively demonstrate that isotropic strengthening the electron density on cathode materials is able to improve the OER activity.

The cells based on MNPs@CNTs (M = Pd and Ru) were further discharged to 1000 mAh g^{-1} and cycled. The charge potential of PdNPs@CNTs as low as 3.94 V (Figure S23) is kept almost for 10 cycles (Figure S24) without significant changes. For RuNPs@CNTs, the corresponding charge potential is 3.86 V (Figure S23), which is also pretty stable upon cycling (Figure S25). SEM observations (Figure S26) reveal that there is no observable "inert" CNTs on RuNPs@CNTs after discharge, and the morphology of Li_2O_2 nanocrystals (10~20 nm) is still pertained although worm-like morphology becomes indistinguishable after covered by substantial amount of Li_2O_2 NPs with increase of discharge depth. Likewise, the PdNPs@CNTs show similar morphology after discharge(Figure S26). Additionally, TEM observations confirm the well preservation of a majority of noble metal NPs inside the CNTs (Figure S27) after cycling. Although encapsulation of noble metal NPs inside CNTs is beneficial for lower charge overpotential, the isotropic distribution of Li_2O_2 on CNTs may also passivate the CNTs surface, leading to a loss of capacity at a deep discharge. Further investigations will focus on these issues. Similar to the results at discharge capacity of 250 mAh g^{-1}, MNPs-CNTs (M = Pd and Ru) exhibit much lower OER activity (Figure S28) with high charge overpotentials (1.6 and 1.6 V, respectively) compared to MNPs@CNTs. The morphology of these electrode materials are still evidenced by the presence of "inert" CNTs and localized aggregation of Li_2O_2 (Figure S29).

3. Conclusion

In the present investigation, we demonstrate that the high charge overpotential can be effectively alleviated by designing CNTs-encapsulated NPs hybrid cathode materials. Encapsulation of nanoparticles significantly strengthens the surface electron density of CNTs without causing regional enrichment of electron density on CNTs surface. Accordingly, the entire surfaces of CNTs serve as catalytic regions for ORR, which ensures uniform covering of Li_2O_2 nanocrystals on CNTs surface. Upon charge, the uniform coverage of Li_2O_2 nanocrystals on CNTs and their intimate contact with CNTs facilitates the decomposition of Li_2O_2 with low charge overpotential, thus result in a dramatic reduction in charge overpotential to 0.3 V. Our findings suggest that tuning the surface electron state of cathode materials is able to optimize the morphology and distribution of Li_2O_2 that is essential for reducing charge overpotential in Li-O_2 batteries.

4. Experimental Section

Chemical reagents were purchased from Sigma-Aldrich and used as received. Raman spectra were obtained with a WITec CRM200 confocal Raman microscopy system with a laser wavelength of 488 nm and a laser spot size of 0.5 mm. The Si peak at 520 cm^{-1} was used as a reference for wavenumber calibration. Morphology of the samples was characterized with a field emission scanning electron microscope (FESEM) system (JEOL, Model JSM-7600F). Transmission electron microscope (TEM) characterizations were performed with a JEOL 2100F operated at 200 kV with energy dispersive X-ray spectroscopy (EDS) attachment. X-Ray Photoelectron Spectroscopy (XPS) of the electrode was performed with an X-ray photoelectron spectrometer (Kratos AXIS Ultra) using monochromatic Al Ka (1486.71 eV) X-ray radiation (15 kV and 10 mA); 160 eV pass energy was used for survey scan, whereas 40 eV was used for the high-resolution scan. ^1H NMR spectra were measured on INOVA 300 MHz NMR spectrometer at ambient temperature. Powder X-ray diffraction (XRD) patterns were recorded with a Bruker AXS D8 Advance diffractometer using nickel-filtered Cu Kα radiation ($\lambda = 1.5406$ Å).

Synthesis of MNPs@CNTs: Multiple wall carbon nanotubes purchased from CNano Technology Ltd. were treated by ball milling in Ar atmosphere for 5 h. The resultant products were denoted as end-opened CNTs. MNPs@CNTs were prepared according to a previously reported method with a slight modification.[45,46] An aqueous solution of precursor salt of Pd ($PdCl_2$), Pt (k_2PtCl_6), Ru ($RuNO(NO_3)_3$) or Au ($HAuCl_4$) was added dropwise in the end-opened CNTs (100 mg) under stirring. The amount of each noble metal was fixed at 10 mg. The precursor solutions fill the end-opened CNTs by capillary forces. The above mixtures were treated by ultrasonication and stirring to aid the filling of precursor solutions in CNTs, and then dried at room temperature. The dried powders were transferred into tubular furnace and heating in Ar/H_2 (H_2, 5%) atmosphere at 200 °C, resulted in CNT encapsulated noble metal nanoparticles, denoted as MNPs@CNT. Based on TEM observation, most of the nanoparticles have been encapsulated inside CNTs, although there are some nanoparticles located at the outer surface of CNTs.

MNPs-CNTs were also prepared by impregnation procedure using pristine CNTs with closed ends to disperse the active nanoparticles.

Electrochemical Measurements: The Li-O_2 battery cells were assembled with a lithium metal anode, electrolyte (1M $LiCF_3SO_3$ in tetraethylene glycol dimethyl ether (TEGDME) impregnated into a glass fibre separator and a porous stainless matrix casted with cathode materials (pristine CNTs, MNPs@CNTs and MNPs-CNTs) as the working electrodes. All cells were assembled in a glove box system filled with Ar (MBraun UniLAB). The concentrations of H_2O and O_2 were both below 0.1 ppm. The battery cells were aerated with O_2 and sealed afterwards, and tested using a NEWARE system with the discharge/charge current density of 50 mA g^{-1}.

Density Functional Theory (DFT) Calculations: The Density functional theory (DFT) calculations were performed by DMol^{3}code in Material Studio. Double numerical plus polarization was taken as the basis set. GGA with the PBE method was utilized as the exchange-correlation functional. The convergence criterion of self-consistent field computations is chosen to be 10^{-5} Ha of the total energy, 0.004Ha/Å for force and 0.005 Å for displacement. The orbital cutoff is set to be global and with the value of 4.0 Å. During the geometry optimization, the coordinates of all the atoms in the CNTs were fully relaxed without any constraint. The simulation models include end-opened (5, 5) single-walled CNT (120 carbon atoms in total) with one Pd (or Pt) atom located inside of the tube [Pd_1@CNT (5, 5), Pt_1@CNT (5, 5)], and end-sealed (5, 5) single-walled CNT with one Pd (or Pt) atom bound on the surface of tube [Pd_1-CNT (5, 5), Pt_1-CNT (5, 5)]. These two types of carbon nanotubes have a similar diameter of 6.8 Å. The model of end-sealed (5, 5) single-walled CNT is represented by a six-layer (60 atoms) stem with each of its mouth capped by half a C_{60} molecule, so the system contains 120 carbon atoms. The length of the open-ended nanotube equals sixth the periodicity of the (5, 5) nanotube, and thus there are totally 120 carbon atoms in the unit cell as well. For the open-ended nanotube, the metal atom was decorated in the inner wall of the nanotube, while it was decorated in the outer wall of the nanotube in the case of end capped nanotube. To obtain the exact and detailed information about the geometrical structures and electronic structures of metal (Pt or Pd)-bound CNTs, a two-step procedure of quantum mechanical calculation was carried out. The doped CNT was first optimized to get the most stable geometrical structure. After that, electronic property calculation was performed.

Supporting Information

Supporting Information is available from the Wiley Online Library or from the author.

Acknowledgments

X. Huang and H. Yu contributed equally to this work. This work was supported by Singapore Ministry of Education MOE AcRF Tier 1 grants RG2/13, A*STAR SERC grant 1021700144, Singapore National Research Foundation under CREATE program: EMobility in Megacities, Singapore MPA 23/04.15.03 RDP 020/10/113 grant, and the USA Air Force Office of Scientific Research for the Project MURI: Synthesis and Characterization of 3-D Carbon Nanotube Solid Networks (FA9550–12–1–0035).

Received: March 21, 2014
Revised: April 1, 2014
Published online: August 22, 2014

---

[1] Z. Y. Guo, D. D. Zhou, X. L. Dong, Z. J. Qiu, Y. G. Wang, Y. Y. Xia, *Adv. Mater.* **2013**, *25*, 5668–5672.
[2] Z. Peng, S. A. Freunberger, Y. Chen, P. G. Bruce, *Science* **2012**, *337*, 563–566.
[3] G. Girishkumar, B. McCloskey, A. C. Luntz, S. Swanson, W. Wilcke, *J. Phys. Chem. Lett.* **2010**, *1*, 2193–2203.
[4] J. J. Xu, Z. L. Wang, D. Xu, L. L. Zhang, X. B. Zhang, *Nat. Commun.* **2013**, *4*, 2438.
[5] J. J. Xu, D. Xu, Z. L. Wang, H. G. Wang, L. L. Zhang, X. B. Zhang, *Angew. Chem. Int. Ed.* **2013**, *52*, 3887–3890.
[6] Y. C. Lu, B. M. Gallant, D. G. Kwabi, J. R. Harding, R. R. Mitchell, M. S. Whittingham, Y. Shao-Horn, *Energy Environ. Sci.* **2013**, *6*, 750–768.
[7] K. M. Abraham, Z. A. Jiang, *J. Electrochem. Soc.* **1996**, *143*, 1–5.
[8] Y. C. Lu, H. A. Gasteiger, M. C. Parent, V. Chiloyan, Y. Shao-Horn, *Electrochem. Solid-State Lett.* **2010**, *13*, A69–A72.
[9] Y. C. Lu, Z. C. Xu, H. A. Gasteiger, S. Chen, K. Hamad-Schifferli, Y. Shao-Horn, *J. Am. Chem. Soc.* **2010**, *132*, 12170–12171.
[10] R. Black, J. H. Lee, B. Adams, C. A. Mims, L. F. Nazar, *Angew. Chem. Int. Ed.* **2013**, *52*, 392–396.
[11] S. H. Oh, R. Black, E. Pomerantseva, J. H. Lee, L. F. Nazar, *Nature Chem.* **2012**, *4*, 1004–1010.
[12] J. S. Hummelshoj, A. C. Luntz, J. K. Norskov, *J. Chem. Phys.* **2013**, *138*, 034703–034712.
[13] A. Debart, A. J. Paterson, J. L. Bao, P. G. Bruce, *Angew. Chem. Int. Ed.* **2008**, *47*, 4521–4524.
[14] L. Jin, L. P. Xun, C. Morein, C. H. Chen, M. Lai, S. Dharmarathna, A. Dobley, S. L. Suib, *Adv. Funct. Mater.* **2010**, *22*, 3373–3382.
[15] G. Q. Zhang, J. P. Zheng, R. Liang, C. Zhang, B. Wang, M. Au, M. Hendrickson, E. J. Plichta, *J. Electrochem. Soc.* **2011**, *158*, A822–A827.
[16] T. H. Yoon, Y. J. Park, *Nanoscale Res. Lett.* **2012**, *7*, 1–4.
[17] A. K. Thapa, K. Saimen, T. Ishihara, *Electrochem. Solid-State Lett.* **2010**, *13*, A165–A167.
[18] Y. C. Lu, H. A. Gasteiger, Y. Shao-Horn, *J. Am. Chem. Soc.* **2011**, *133*, 19048–19051.
[19] J. R. Harding, Y. C. Lu, Y. Tsukada, Y. Shao-Horn, *Phys. Chem. Chem. Phys.* **2012**, *14*, 10540–10546.
[20] B. D. McCloskey, R. Scheffler, A. Speidel, D. S. Bethune, R. M. Shelby, A. C. Luntz, *J. Am. Chem. Soc.* **2011**, *133*, 18038–18041.
[21] J. S. Hummelshoj, A. C. Luntz, J. K. Norskov, *J. Chem. Phys.* **2013**, *138*, 034703–034712.
[22] R. R. Mitchell, B. M. Gallant, Y. Shao-Horn, C. V. Thompson, *J. Phys. Chem. Lett.* **2013**, *4*, 1060–1064.
[23] B. M. Gallant, R. R. Mitchell, D. G. Kwabi, J. G. Zhou, L. Zuin, C. V. Thompson, Y. Shao-Horn, *J. Phys. Chem. C* **2012**, *116*, 20800–20805.
[24] Y. C. Lu, H. A. Gasteiger, E. Crumlin, R. McGuire, Y. Shao-Horn. *J. Electrochem. Soc.* **2010**, *157*, A1016–A1025.
[25] J. S. Lee, S. T. Kim, R. G. Cao, N. S. Choi, M. Liu, K. T. Lee, J. Cho, *Adv. Energy Mater.* **2011**, *1*, 34–50.
[26] H. L. Wang, Y. Yang, Y. Y. Liang, G. Y. Zheng, Y. G. Li, Y. Cui, H. J. Dai, *Energy Environ. Sci.* **2012**, *5*, 7931–7935.
[27] T. Ogasawara, A. Debart, M. Holzapfel, P. Novak, P. G. Bruce, *J. Am. Chem. Soc.* **2006**, *128*, 1390–1393.
[28] Y. H. Chen, S. A. Freunberger, Z. Q. Peng, O. Fontaine, P. G. Bruce, *Nature Chem.* **2012**, *4*, 1004–1010.
[29] S. D. Beattie, D. M. Manolescu, S. L. Blair, *J. Electrochem. Soc.* **2009**, *156*, A44–A47.
[30] G. Q. Zhang, J. P. Zheng, R. Liang, C. Zhang, B. Wang, M. Hendricksone, E. J. Plichta, *J. Electrochem. Soc.* **2010**, *157*, A953–A956.
[31] R. R. Mitchell, B. M. Gallant, C. V. Thompson, Y. Shao-Horn, *Energy Environ. Sci.* **2011**, *4*, 2952–2958.
[32] T. Fujimori, A. Morelos-Gomez, Z. Zhu, H. Muramatsu, R. Futamura, K. Urita, M. Terrones, T. Hayashi, M. Endo, S. Y. Hong, Y. C. Choi, D. Tomanek, K. Kaneko, *Nat. Commun.* **2013**, *4*, 2162.
[33] Z. Q. Yang, S. J. Guo, X. L. Pan, J. H. Wang, X. H. Bao, *Energy Environ. Sci.* **2011**, *4*, 4500–4503.
[34] A. M. Rao, P. C. Eklund, S. J. Bandow, A. Thess, R. E. Smalley, *Nature* **1997**, *388*, 257–259.
[35] W. Chen, X. L. Pan, X. H. Bao, *J. Am. Chem. Soc.* **2007**, *129*, 7421–7426.
[36] C. L. Jiang, S. Ranjit, Z. Y. Duan, Y. L. Zhong, K. P. Loh, C. Zhang, X. G. Liu, *Nanoscale* **2009**, *1*, 391–394.
[37] S. Santra, P. Ranjan, P. Bera, P. Ghosh, S. K. Mandal, *RSC Adv.* **2012**, *2*, 7523–7533.
[38] J. Kim, J. Lee, Y. Tak, *J. Power Sources* **2009**, *192*, 674–678.
[39] W. Y. Zhang, J. X. Zhu, H. X. Ang, Y. Zeng, N. Xiao, Y. B. Gao, W. L. Liu, H. H. Hng, Q. Y. Yan, *Nanoscale* **2013**, *5*, 9651–9658.
[40] J. S. Hummelshoj, J. Blomqvist, S. Datta, T. Vegge, J. Rossmeisl, K. S. Thygesen, A. C. Luntz, K. W. Jacobsen, J. K. Norskov, *J. Chem. Phys.* **2010**, *132*, 071101.
[41] M. Radin, F. Tian, D. Siegel, *J. Mater. Sci.* **2012**, *47*, 7564–7570.
[42] M. D. Radin, J. F. Rodriguez, F. Tian, D. J. Siegel, *J. Am. Chem. Soc.* **2012**, *134*, 1093–1103.
[43] Y. Xu, W. A. Shelton, *J. Electrochem. Soc.* **2011**, *158*, A1177–A1184.
[44] D. H. Deng, L. Yu, X. Q. Chen, G. X. Wang, L. Jin, X. L. Pan, J. Deng, G. Q. Sun, X. H. Bao, *Angew. Chem. Int. Ed.* **2013**, *52*, 371–375.
[45] X. L. Pan, Z. L. Fan, W. Chen, Y. J. Ding, H. Y. Luo, X. H. Bao, *Nature Mater.* **2007**, *6*, 507–511.
[46] S. J. Guo, X. L. Pan, H. L. Gao, Z. Q. Yang, J. J. Zhao, X. H. Bao, *Chem. Eur. J.* **2010**, *16*, 5379–5384.